Shape control of colloidal $Cu_{2-x}S$ polyhedral nanocrystals by tuning the nucleation rates

Shape Control of Colloidal $Cu_{2-x}S$ Polyhedral Nanocrystals by Tuning the Nucleation Rates

Ward van der Stam[†], Sabine Gradmann[‡], Thomas Altantzis[§], Xiaoxing Ke[§], Marc Baldus[‡], Sara Bals[§], and Celso de Mello Donega*[†]

†Condensed Matter and Interfaces, Debye Institute for Nanomaterials Science, Utrecht University, P.O. Box 80000, 3508 TA Utrecht, The Netherlands

‡NMR Spectroscopy, Bijvoet Center for Biomolecular Research, Department of Chemistry, Faculty of Science, Utrecht University, Padualaan 8, 3584 CH Utrecht, The Netherlands

§ EMAT, University of Antwerp, Groenenborgerlaan 171, B-2020 Antwerp, Belgium

ABSTRACT: Synthesis protocols for colloidal nanocrystals (NCs) with narrow size and shape distributions are of particular interest for the successful implementation of these nanocrystals into devices. Besides, the preparation of NCs with well-defined crystal phases is of key importance. In this work, we show that Sn(IV)-thiolate complexes formed *in-situ* strongly influence the nucleation and growth rates of colloidal $Cu_{2-x}S$ polyhedral NCs, thereby dictating their final size, shape, and crystal structure. This allowed us to successfully synthesize hexagonal bifrustums and hexagonal bipyramid NCs with the low-chalcocite crystal structure, and hexagonal nanoplatelets with various thicknesses and aspect ratios with the djurleite crystal structure, by solely varying the concentration of Sn(IV)-additives (*viz*., $SnBr_4$) in the reaction medium. Solution and solid-state ^{119}Sn-NMR measurements show that $SnBr_4$ is converted *in-situ* to Sn(IV)-thiolate complexes, which increase the $Cu_{2-x}S$ nucleation barrier, without affecting the precursor conversion rates. This influences both the nucleation and growth rates in a concentration dependent fashion, and leads to a better separation between nucleation and growth. Our approach of tuning the nucleation and growth rates with *in-situ* generated Sn-thiolate complexes might have a more general impact, due to the availability of various metal-thiolate complexes, possibly resulting in polyhedral NCs of a wide variety of metal-sulfide compositions.

INTRODUCTION

In recent years, the scientific community has achieved a high level of mastery over the size, shape and composition of colloidal nanocrystals (NCs) and heteronanocrystals (HNCs) of Cd- and Pb-chalcogenide compositions.[1–4] However, their further deployment into applications has been hindered by toxicity concerns.[5–8] The properties of copper chalcogenides ($Cu_{2-x}A$, with A = S, Se and Te) make them attractive alternatives for Cd- and Pb-based semiconductors for several applications.[6,8–10] For instance, $Cu_{2-x}S$ is a direct p-type semiconductor with a band gap that depends on its stoichiometry (1.1 - 1.4 eV for x = 0 – 0.04; 1.5 eV for x = 0.2; 2.0 eV for x = 1).[11–13] The combination of a suitable band gap, high absorption coefficient (10^4 cm^{-1}), low cost, and low toxicity has made $Cu_{2-x}S$ a promising candidate for large scale and sustainable implementation into photovoltaic (PV) devices.[14,15] Moreover, $Cu_{2-x}A$ NCs can hold both excitons and tunable localized surface plasmon resonances on demand.[9,13,16–18] This makes $Cu_{2-x}A$ NCs promising materials for photovoltaics,[15] photocatalysis,[19] sensing[20] and nanoplasmonics.[9,11,17,21,22]

The application of colloidal NCs in photovoltaic and nanoplasmonic devices requires strict control over the size, shape and polydispersity of the NC ensemble, since these characteristics are of crucial importance not only for the optoelectronic properties of the NCs themselves, but also for the quality of the NC thin films obtained by solution based deposition techniques.[23–25] $Cu_{2-x}S$ NCs are of particular interest, since a variety of shapes not attainable for other semiconductor NCs can easily be synthesized with narrow size and shape distributions. For example, hexagonal nanodisks, nanoplatelets and nanosheets, among other polyhedral shapes, have been successfully synthesized.[6,26–29] Shape control over $Cu_{2-x}S$ NCs may also have a more general impact, since Cu^+ ions in copper chalcogenides have been shown to be easily exchangeable by other cations.[6,30–37] This opens up the possibility of using (partial) topotactic cation exchange reactions to convert $Cu_{2-x}A$ NCs into other compositions, while preserving the size and shape of the parent NCs, thereby making NCs with novel functionalities.[33,36,37] However, the methods currently available to control the size and shape of $Cu_{2-x}S$ NCs lack flexibility, since different sets of physical-chemical parameters (concentrations, ligands, reaction temperatures, reaction

times) have to be used for each different shape.[6,26,28] In this work, a novel methodology for the size and shape control of colloidal $Cu_{2-x}S$ NCs is developed, which relies on changing just one single reaction variable: the concentration of Sn(IV)-complexes that are used to control the nucleation and growth rates of $Cu_{2-x}S$ NCs. In this way, hexagonal bifrustums, hexagonal bipyramids and hexagonal nanoplatelets of various aspect ratios are synthesized with narrow size and shape distributions. Solid-state ^{119}Sn-NMR measurements indicate that Sn-thiolate complexes formed *in-situ* control the nucleation and growth rates, which results in various polyhedral $Cu_{2-x}S$ NCs. Our study provides insights into the formation of polyhedral $Cu_{2-x}S$ NCs and possibly paves the way toward the development of synthetic protocols for polyhedral NCs of various compositions by deployment of *in-situ* nucleation and growth controlling agents, such as Sn(IV)-thiolates.

EXPERIMENTAL SECTION

Colloidal hexagonal bipyramid-shaped $Cu_{2-x}S$ NCs were synthesized based on the protocol described by Kuzuya *et al.*,[38] which was modified by adding $SnBr_4$ to the reaction mixture. In a typical synthesis, 1.0 mmol CuCl (99 mg) and 0.5 mmol $SnBr_4$ (219 mg) were mixed in 8 mL (33.6 mmol) of 1-dodecanethiol (DDT) and 2 mL (6 mmol) of oleylamine (OLAM). The flask was purged with N_2 and the solution was gradually heated to 225 °C. At first, a creamy white substance was present, but around 80 °C the solution turned slightly yellow. When further heated, a clear yellow solution was obtained around 130 °C. Nucleation and growth of $Cu_{2-x}S$ started when the temperature had reached 200 °C. Finally, the particles were allowed to grow at 225 °C for one hour and subsequently the nanoparticles were precipitated by the repeated addition of a methanol/butanol solution and redispersion in toluene.

Colloidal polyhedral $Cu_{2-x}S$ NCs of various morphologies were synthesized based on the same method as described above, only the amount $SnBr_4$ was varied (Cu:Sn ratio of 2:3 for low aspect ratio hexagonal nanoplatelets, 1:2 for high aspect ratio hexagonal nanoplatelets, 30:1 for small hexagonal bifrustums and 1:1 for large hexagonal bipyramids).

Transmission Electron Microscopy (TEM) and Energy Dispersive X-Ray Spectroscopy (EDS). TEM and EDS measurements were performed on a Tecnai20F (FEI) microscope equipped with a Field Emission Gun, a Gatan 694 CCD camera and an EDAX spectrometer. The microscope was operated at 200 kV. Acquisition time for EDS measurements was 30 s. Samples for TEM imaging were prepared by dripping a diluted nanocrystal solution in toluene on a carbon coated polymer film copper grid (300 mesh). The solvent (toluene) was allowed to evaporate prior to imaging.

High-resolution (Scanning) Transmission Electron Microscopy measurements were performed on a double aberration corrected cubed FEI Titan 50-80 electron microscope operated at 120 kV. High-resolution Transmission Electron Microscopy measurements were performed on a FEI Osiris and a FEI Tecnai electron microscopes operated at 200 kV. Electron tomography measurements were performed in High-Angle Annular Dark-Field Scanning Transmission Electron Microscopy (HAADF-STEM) mode, in order to get rid of any unwanted diffraction contrast present in TEM, by using an aberration-corrected cubed FEI Titan 60-300 electron microscope and a double aberration-corrected cubed FEI Titan 50-80 electron microscope operated at 200 and 300 kV. The acquisition of all the series was performed manually over a tilt range from -74° to +74° and a tilt increment of 2° by using a Fischione model 2020 single tilt tomography holder. The alignment of all the acquired series was performed by using cross-correlation and the reconstruction by using the Simultaneous Iterative Reconstruction Technique (SIRT) as implemented in ASTRA toolbox.[74]

Solid-state ^{119}Sn-NMR & solution ^{1}H-NMR experiments were performed using a Bruker Avance III spectrometer equipped with a 4 mm double resonance probehead at 11.7 T static magnetic field. All experiments on precipitated and dry nanocrystals were measured at room temperature and on solution samples at 308 K. Tin and proton field strengths for 90° pulses were 50 kHz and 71 kHz, respectively. Spectral referencing was done using $SnBr_4$ for tin and adamantane for protons. For solution ^{119}Sn-NMR and ^{1}H-NMR measurements, no additional solvents were added. The crude reaction mixture was loaded in a capillary at elevated temperatures, and subsequently cooled to room temperature before measurement. No precipitation was observed upon cooling.

X-Ray Diffraction (XRD) patterns were obtained by using a PW 1729 Philips diffractometer, equipped with a Cu K_α X-ray source (λ = 1.5418 Å). Samples for XRD analysis were prepared by depositing purified NCs on a Si wafer substrate under inert atmosphere. The purification procedure consisted of precipitating the NCs from a solution of NCs in toluene by adding anhydrous methanol (1:1 volume ratio). The sediment was isolated by centrifugation (3000 rpm, 15 min) and redispersed in chloroform. The concentrated solution of NCs was dropcasted op the Si wafer and the chloroform was allowed to evaporate at RT, resulting in a concentrated NC solid.

RESULTS AND DISCUSSION

Shape control of anisotropic $Cu_{2-x}S$ NCs by $SnBr_4$ addition. Colloidal $Cu_{2-x}S$ NCs were synthesized by heating up a solution of CuCl in 1-dodecanethiol (DDT) and oleylamine (OLAM) to 225 °C. In this protocol, DDT has the combined roles of ligand, solvent and sulfur source.[38–40] In the absence of $SnBr_4$ large polydisperse nanoplatelets (~100 nm lateral dimensions) are obtained (Figure 1a). The addition of $SnBr_4$ to the reaction mixture

has a dramatic impact on the size and shape of the product NCs, leading to a variety of polyhedral shapes (hexagonal bifrustums, hexagonal bipyramids, low and high aspect ratio hexagonal nanoplatelets) with small polydispersity, depending on the $SnBr_4$ concentration (Figure 1).

High-Resolution Transmission Electron Microscopy (HRTEM) (Figure 2), Electron Diffraction (Supporting Information, Figure S1) and X-ray Diffractometry (Supporting Information, Figure S2) measurements revealed that the product $Cu_{2-x}S$ nanoplatelets have the djurleite crystal structure,[41] whereas the product $Cu_{2-x}S$ bipyramids have the low-chalcocite crystal structure. This is evident in the HRTEM images and the corresponding Fast Fourier Transform (FFT) patterns of hexagonal bipyramid NCs viewed along the [010] zone axis (Figure 2a,d, and Supporting Information, Figure S3), and of low aspect ratio nanoplatelets (Figure 2b,c,e,f). The observed spacings are in agreement (within a 1% error margin) with the djurleite crystal structure (lattice parameters a = 26.89 Å, b = 15.74 Å and c = 13.57 Å)[41] for the nanoplatelets and with the low-chalcocite crystal structure (lattice parameters a = 11.92 Å, b = 27.34 Å and c = 13.44 Å)[41] for the bipyramid NCs.

The morphology of the NCs was investigated by carrying out electron tomography measurements in High-Angle Annular Dark Field Scanning Transmission Electron Microscopy (HAADF-STEM) mode (Figure 3). By combining the electron tomography results, which enabled the determination of the shape of the NCs, with the crystallographic information obtained by the HRTEM analysis (Figure 2 above), the different facets can be indexed according to the monoclinic low-chalcocite (for bipyramids) and monoclinic djurleite (for nanoplatelets) crystal structures.[41] In this way, the lateral facets of the low-chalcocite bipyramids are indexed as {364} (8 facets), {502} (2 facets) and {302} (2 facets) (Figure 3b,c). A different indexation holds for the low and high aspect ratio hexagonal nanoplatelets, which have the djurleite crystal structure. The side facets of the nanoplatelets are formed by 8 trapezoidal {221} and 4 {101} facets, and the top and bottom facets are the hexagonal {100} facets. It is thus evident that the addition of $SnBr_4$ alters the size and crystal structure, and hence, the faceting, of $Cu_{2-x}S$ NCs in a concentration dependent fashion. At the lowest Cu:Sn ratio (30:1) small (d = 17 nm) hexagonal bifrustums are obtained with the low-chalcocite crystal structure, in which the top and bottom {102} facets and the {364} and {302}/{502} side facets have similar areas. Increase of the Cu:Sn ratio to 2:1 leads to large (28 nm by 38 nm), hexagonal bipyramidal low-chalcocite NCs in which the {102} facets are almost absent. Further increase of the Cu:Sn ratio results in djurleite hexagonal nanoplatelets of which the relative area of the {100} facets, the lateral dimensions and the aspect ratio grow with the Cu:Sn ratio (25 nm thick, 50 nm wide, for Cu:Sn = 2:3; and 10 nm thick, 80 nm wide, for Cu:Sn = 1:2). The formation mechanism for low-chalcocite bipyramids and djurleite nanoplatelets will be discussed in detail below.

Our group has previously reported that the addition of $SnBr_4$ to synthesis protocols for $Cu_{2-x}S$ NCs dramatically affects the size and shape of the product NCs, yielding ultrathin (2 nm thick) $Cu_{2-x}S$ nanosheets with well-defined shape and size (triangular or hexagonal, 100 nm to 3 μm wide), instead of nearly spherical small (9 nm diameter) NCs.[29] The effect was clearly shown to be due to the halides, so that Sn(IV) tetrahalides were only relevant as sources of sufficiently high halide concentrations in the growth solution.[29] To investigate the roles of the halide and Sn(IV) in the present case, we carried out control experiments, in which either $SnBr_4$ was replaced by $Sn(OAc)_4$ or additional halides were added in the form of CuBr in the absence of any Sn(IV) compound. The results clearly show that, in contrast to our previous study on the formation of ultrathin $Cu_{2-x}S$ nanosheets,[29] the effect in the present case is due to the Sn(IV) (Supporting Information, Figure S4), since additional halides yield polydisperse nanoplatelets similar to those obtained under the standard reaction conditions (*i.e.*, $SnBr_4$ absent, Figure 1a above), while addition of $Sn(OAc)_4$ resulted in polyhedral NCs similar to those obtained upon addition of $SnBr_4$ (Cu:Sn= 2:1, Figure 1c above). We wish to note that the polydispersity of the polyhedral NCs obtained by adding $Sn(OAc)_4$ has increased compared to the polyhedral NCs formed upon the addition of $SnBr_4$. The larger polydispersity observed when using $Sn(OAc)_4$ instead of $SnBr_4$ can be ascribed to the fact that $Sn(OAc)_4$ is less reactive toward DDT molecules than $SnBr_4$, since acetate and Sn^{4+} are a strong Lewis base and acid, respectively, and are better matched in terms of hardness (both hard) than bromide and Sn^{4+} (soft and hard, respectively).[42] This suggests that the active Sn(IV) species responsible for the observed morphological changes result from a reaction between DDT and the added Sn(IV) salt. This also explains the different roles observed for Sn(IV) in the present work (active species) and in our previous study on the formation of $Cu_{2-x}S$ nanosheets (*viz.*, halide carrier),[29] since in the latter case a smaller excess of DDT (10-fold with respect to Cu) was injected in the reaction mixture, while in the present case a large excess of DDT is used (30-fold with respect to Cu), allowing the formation of both Cu-DDT and Sn-DDT complexes, despite the lower reactivity of Sn(IV) toward DDT. Furthermore, in our previous work, the Cu-thiolate precursor complexes were diluted in a poor solvent (1-octadecene) which presumably increased the reactivity of Cu^+ toward DDT. As will become clear below (NMR Spectroscopy section), another important chemical difference in the present reaction system is the presence of oleylamine, which deprotonates DDT, thereby further facilitating its reaction with $SnBr_4$.

To gain further insight into the role of $SnBr_4$ in the shape control of the product $Cu_{2-x}S$ NCs, Energy Dispersive X-ray spectroscopy (EDS) chemical mapping was used to quantify and locate the elements present in the NCs. The Cu:Sn:S ratio was found to be 1.81±0.14: 0.02±0.01: 1.00, regardless of the Cu:Sn ratio used in the

reaction. Bromide was not detected in any sample. Elemental mapping shows that Sn is not homogeneously distributed across the ensemble of NCs, but is concentrated on a few NCs that appear morphologically distinct from the majority of the ensemble (Supporting Information, Figures S5 and S6). The Sn distribution in the Sn-poor NCs does not indicate any preference for a particular facet, regardless of the shape of the NC (*i.e.*, bipyramids or nanoplatelets, Supporting Information, Figures S5 and S6, respectively). The signal from individual NCs was too low to allow the composition of the Sn-rich NCs to be reliably established, but their different shapes imply that they no longer have the hexagonal crystal structure of djurleite or low-chalcocite,[41] and may have adopted the cubic crystal structure characteristic of ternary $Cu_xSn_yS_z$ phases (*e.g.*, zinc blende for Cu_2SnS_3, cubic spinel for $Cu_2Sn_3S_7$).[43–46] The Cu-Sn-S phase diagram is however quite rich (16 different phases, 13 of them metastable),[46] and therefore the range of possible compositions for the Sn-rich NCs is very wide (from $Cu_9Sn_2S_9$ to $Cu_2Sn_{3.75}S_8$). Nevertheless, it is clear that in these NCs some degree of Sn(IV) inter-diffusion has taken place, inducing crystal structure and morphology changes. Considering that only a very small fraction of the NCs is observed to be Sn-rich (<5%), we can conclude that the Sn(IV)-diffusion rates in the $Cu_{2-x}S$ NCs were negligible under the conditions prevalent in our experiments. This is consistent with previous studies in which significant Sn(IV) inter-diffusion in $Cu_{2-x}S$ NCs was only observed at temperatures as high as 240 °C.[45] Other studies on the nucleation and growth of multinary Cu chalcogenide compounds (such as $CuInS_2$, Cu_2SnS_3 and Cu_2ZnSnS_4) have shown that binary Cu_2S nucleates first, after which the other cations diffuse into the existing seeds.[45,47,48] Therefore, we exclude separate nucleation events as a possible explanation for the observed Cu-Sn-S NCs.

The results presented above clearly demonstrate that the impact of $SnBr_4$ in the size and shape evolution of $Cu_{2-x}S$ NCs synthesized by heating-up a solution of CuCl in DDT is due to *in-situ* generated Sn(IV) species, and rules out Sn(IV) incorporation as the cause for the observed changes. To uncover the nature of the Sn(IV)-complexes that were formed *in-situ* and to verify whether they bind to the surface of the $Cu_{2-x}S$ NCs, we carried out ^1H and ^{119}Sn NMR spectroscopic measurements.

Solution and solid-state NMR Spectroscopy. ^{119}Sn NMR spectroscopy is particularly suited to elucidate the nature of the Sn-complexes in solution and on the surface of the NCs. Overall, the fairly high natural abundance of ^{119}Sn nuclei as well as the large range of isotropic chemical shifts (around 6500 ppm) that leads to clearly separated chemical shift regions in the spectra, makes ^{119}Sn NMR a promising tool for characterizing tin compounds. Combined with novel NMR methods like dynamic nuclear polarization (DNP) ^{119}Sn NMR also has a great potential for the investigation of nanomaterial surfaces.[49] Furthermore, former studies have shown that the chemical shift tensor parameters of tin sulfides are highly sensitive to coordination numbers and symmetry in the local environment of the tin atom.[50] Therefore, probing the chemical shift anisotropy (CSA) *via* solid-state NMR provides an opportunity to detect structural details.

In the following, three of our $Cu_{2-x}S$ NC morphologies were analyzed with solid-state ^{119}Sn NMR, namely the hexagonal bipyramids (Cu:Sn 2:1), the low aspect ratio nanoplatelets (Cu:Sn 2:3) and the high aspect ratio nanoplatelets (Cu:Sn 1:2). The reference for solid-state ^{119}Sn NMR measurements was $SnBr_4$, with a sharp peak at chemical shift δ -638 ppm. None of the measured NC samples showed a detectable amount of $SnBr_4$ in the spectra. Instead, in the cases of an excess of Sn compared to Cu, the spectra were dominated by a sharp signal at 144 ppm under static conditions as well as magic angle spinning (MAS) at 5 kHz (black lines in Figure 4b, signal at 144 ppm indicated with a red star, see also Supporting Information Figure S7). The fact that there is no line narrowing after spinning at 5 kHz indicates that these compounds have a symmetrical surrounding, meaning they are not on the NC surface.[50] Additionally, less intense and broader signals in the chemical shift range between 0-80 ppm were observed for the high aspect ratio $Cu_{2-x}S$ NPs, obtained by mixing Cu(I) and Sn(IV) salts in a 1:2 ratio (Figure 4b, indicated with blue stars). In the presence of a higher Cu amount compared to Sn (Cu:Sn 2:1, bipyramids), one broad peak centered at -208 ppm was detected (top of Figure 4b, indicated with a black star, see also Supporting Information Figure S7c). Here, 5 kHz spinning resulted in significant line narrowing (top ofFigure 4b), indicating an asymmetrical surrounding. This signal was therefore assigned to a Sn-compound bound to the NC surface. Comparison with the chemical shift values reported by Kovalenko *et al.*[51,52] for Sn-sulfocomplexes ($[Sn_2S_6]^{4-}$ and $[SnS_4]^{4-}$ at δ 56.3 ppm and δ 70-75 ppm, respectively) lead to the conclusion that the Sn(IV) species formed *in-situ* in our experiments are of a different nature. This is further supported by the fact that the anisotropic line broadening (around 60 ppm, top of Figure 4b) of the ^{119}Sn NMR spectrum obtained for hexagonal bipyramids (Cu:Sn of 2:1) is far less pronounced than reported in literature for salts containing $[Sn_2Sn_6]^{4-}$ ions.[53]

We thus propose a mechanism where thiol molecules replace bromides from $SnBr_4$ in order to form Sn-thiolate complexes. This replacement is a stepwise process, where one Br is replaced by a thiol in each step (Figure 4a). Tin(IV) methylthiolate, $(MeS)_4Sn$, is known to show a sharp signal at 160 ppm.[54,55] A shift to slightly lower ppm values is expected if the methylthiolate groups are replaced by thiolate-groups containing longer alkyl chains,[54,55] as dodecylthiolate in the present work. The sharp signal at 144 ppm is thus assigned to $(C_{12}H_{25}S)_4Sn$ (indicated by a red star in panel a). This interpretation is supported by earlier findings that related sharp signals with a lack of prominent sidebands under slow spinning speeds (around 3 kHz) and low magnetic fields correspond to salts containing $[SnS_4]^{4-}$ compounds.[50] The

clear contribution of anisotropic chemical shielding (CSA) interactions to the broad signal at -208 ppm indicates a non-isotropic environment of the central tin atom (Figure 4a, indicated by a black star). The lower ppm value compared to the sharp peak at 144 ppm suggests the presence of remaining Br atoms, since the quadrupolar nature of ^{79}Br and ^{81}Br would further contribute to the line broadening. Previous studies have shown that a successive replacement of Br *via* alkyls in tin compounds leads to a large, non-linear shift towards higher ppm values (*e.g.* $MeSnBr_3$ -165 ppm, Me_2SnBr_2 70ppm, Me_3SnBr 128 ppm).[52] Bearing these values in mind, we attribute the signal at -208 ppm to the intermediate compound $(C_{12}H_{25}S)SnBr_3$.

Further, ^{119}Sn NMR was also used to analyze the compounds present in solution prior to the onset of $Cu_{2-x}S$ NC nucleation (Figure 4c). To this end, CuCl and $SnBr_4$ were mixed in different Cu:Sn ratios (2:1 for hexagonal bipyramids, 2:3 for low aspect ratio nanoplatelets and 1:2 for high aspect ratio hexagonal NPs, blue lines in Figure 4c, see also Supporting Information Figure S7) in a DDT/OLAM solution and heated to 180 °C. This temperature is slightly below the onset of $Cu_{2-x}S$ NC nucleation (~220 °C), which gives rise to the formation of all precursors, without (significant) formation of $Cu_{2-x}S$ nuclei. The dominating peak at 144 ppm is present in solution as well (blue lines in Figure 4c) and a second Sn-complex is observed around 80 ppm (indicated with a blue star). Furthermore, solution samples without Cu^+ ions (red lines in Figure 4c, see also Supporting Information Figure S7) show the same signal at 144 ppm (indicated with a red star). This finding demonstrates that the formation of the compound responsible for the peak at 144 ppm is independent of the presence of Cu^+ or NCs, so this peak can be unambiguously ascribed to unbound $(C_{12}H_{25}S)_4Sn$. However, additional peaks in the range of 80-0 ppm show a clear dependency on the presence of Cu^+ (peaks indicated with a blue star, only observed when Cu(I) and Sn(IV) are present simultaneously). This suggests that a thiolate complex containing both Sn(IV) and Cu(I) is present prior to the onset of $Cu_{2-x}S$ nucleation. Heterometallic polynuclear Sn(IV)-Cu(I) complexes in which thiolates act as ligands are known to be stable both in solution and as crystalline solids.[56,57] It is thus plausible that similar complexes are also formed during the heating-up of the reaction medium to the reaction temperature. Although the chemical shift values are slightly different, the signals observed in the pre-nucleation solutions at 80 ppm and in the solid-state samples of high aspect ratio nanoplatelets (Cu:Sn ratio 1:2) at 80-0 ppm might have the same origin. Different packing in the solid state and different coordination modes in solution could be a possible explanation for the differences, as it has already been reported for other tin(IV) compounds before.[58]

For further investigation, we performed ^1H-NMR measurements on the solution and solid-state samples (Supporting information, Figure S8 and S9). All three spectra for solution samples show huge proton density at chemical shift areas characteristic for alkyl chains (3.5-0 ppm) and a peak at around 5 ppm, which typically corresponds to an $R\text{-}NH_3^+$ species (Figure S8, Supporting Information). This implies that the amine group of OLAM deprotonates the thiol head group of DDT, resulting in nucleophiles ($C_{12}H_{25}S^-$) that are more reactive toward both Sn(IV) and Cu(I). This is consistent with our experimental observation that the presence of OLAM increases the reaction rates. Furthermore, a peak is observed around 7.5-8 ppm, which can be ascribed to the presence of Sn, since it is absent in the case of the Cu-DDT/OLAM solution (*i.e.* when no Sn is present in the reaction medium).

Copper sulfide NCs prepared with thiols as sulfur source are shown to be resistant to ligand exchange procedures. Recent study by Turo and Macdonald[59] provided strong evidence that when thiols are used as sulfur source, they not only bind to the surface of the product $Cu_{2-x}S$ nanocrystals by interaction with cations at low coordination number surface sites ("surface-bound thiols), but are also effectively integrated in the NC ("crystal-bound thiols), forming the terminal sulfur layers of the crystal and occupying high coordination number sites. These strongly bound thiols explain why ligand exchange is difficult. Oleylamine capped $Cu_{2-x}S$ NCs can only be obtained in the absence of DDT (*i.e.* using sulfur powder as S-source). Furthermore, OLAM is easily exchanged by DDT by post-synthetic ligand exchange. 1H NMR measurements are not suitable to discriminate between "surface-bound thiols" and "crystal-bound thiols", since the signals from the alkylchains are unsufficiently different, resulting in small changes in the chemical shift of the signals. Amines have been also shown to strongly bind to the surface of Cu chalcogenide nanomaterials, such as $CuInS_2$ and Cu_2ZnSnS_4 NCs.[59-61] In these works, surface bound amines are characterized by broad signals in the 1H-NMR spectra. Our solid-state and solution 1H-NMR spectra provide no evidence for surface bound amines (Supporting Information, Figure S8 and S9), due to the lack of broadening in the spectra. The only broad signal observed corresponds to $R\text{-}NH_3^+$ species around 5 ppm. Broadening of thiol signals are hard to assign, due to the high proton density corresponding to free thiol molecules which give rise to signals at comparable chemical shift. Besides, based on hard-soft-acid-base theory, a higher affinity of thiols for surface Cu is expected due to their similar chemical hardness (η ~6 eV).[42] Therefore, we infer that in our case, thiols cover the surface of the polyhedral $Cu_{2-x}S$ NCs and the amines have the adjuvant role of deprotonating the thiol head group (as described above).

Mechanism. Based on the findings discussed above, we propose a mechanism for the impact of $SnBr_4$ and other Sn(IV) salts (*e.g.*, $Sn(OAc)_4$, $SnCl_4$, $Sn(acetylacetonate)Cl_2$) on the size, shape and crystal structure evolution of $Cu_{2-x}S$ NCs formed by heating up Cu salts in DDT. First, the thiolate complexes of both Cu(I) and Sn(IV) (Cu(DDT) and $Sn(DDT)_4$, respectively)

are formed by replacement of the native anions by DDT. This reaction is facilitated by amines (OLAM in the present case), which deprotonate the thiol, forming a nucleophile that is sufficiently reactive to displace the native anions bound to Sn(IV). Our results (see NMR spectroscopy section above) show that the replacement of Br by DDT occurs in a stepwise fashion, one Br at a time, until the fully substituted $(C_{12}H_{25}S)_4Sn$ complex is formed. The stability of Cu(I)-DDT is known to be higher than that of Cu(II)-DDT[62] and therefore, when Cu(II) salts are used, the formation of the Cu-DDT complex is preceded by the reduction of Cu(II) to Cu(I) by oxidation of DDT to didodecyl disulfide.[40]

Copper(I) thiolates are very useful as single-source precursors for the synthesis of $Cu_{2-x}S$ NCs, and have been extensively used for that purpose, both in solventless and solution based routes using either hot-injection or heating-up protocols.[6,26,29,38–40,63,64] The rate limiting step in the formation of $Cu_{2-x}S$ NCs from Cu(I)-thiolates has been shown to be the thermally induced cleavage of the C-S bond,[40] which is catalyzed by the Cu(I) atoms,[65] so that only DDT molecules directly bound to Cu undergo thermolysis. In order for [Cu-S] monomers to be formed, several C-S bonds must be cleaved, since each Cu-atom is coordinated to four DDT molecules.[62] It is interesting to note that the observations discussed above imply that the reaction temperature used in our study (225°C) is sufficiently high to lead to thermolysis of Cu-thiolate, followed by nucleation and growth of $Cu_{2-x}S$ NCs, but is too low to induce significant thermolysis of the C-S bonds of the Sn(IV) thiolate complexes, since $[Sn_xS_y]^{n-}$ species are not observed. Instead, our study demonstrates that the active species are $Sn(DDT)_4$ and/or the partially substituted complexes, such as $Sn(DDT)Br_3$. The high thermal stability of $Sn(DDT)_4$ is in line with the high decomposition temperatures reported for tin(IV) thiolates and dithiocarbamates, which require temperatures ranging from 250 to 375 °C to yield SnS_2.[66]

To understand how the $Sn(DDT)_xBr_y$ (x= 1-4; y= 0-3) complexes generated *in-situ* affect the size and shape evolution of the $Cu_{2-x}S$ NCs, we have to consider the formation mechanism of colloidal $Cu_{2-x}S$ NCs upon heating-up of a solution of CuCl in excess DDT. As discussed above, Cu-DDT is initially formed, which is followed at sufficiently high temperatures by thermolysis of the C-S bonds of the Cu-DDT complex, thereby forming [Cu-S] monomers. As a result of the high activation energies associated with the C-S bond cleavage, the precursor to monomer formation becomes the rate-limiting step in the formation of $Cu_{2-x}S$ NCs from Cu-DDT.[6,40] This is in line with the general mechanism proposed for the formation of colloidal NCs of several metal chalcogenides (*e.g.*, CdSe, PbSe, PbS),[1,67–69] and implies that tuning the precursor conversion kinetics can dramatically affect the nucleation and growth rates, allowing the size, shape and crystal structure of the nanocrystals to be controlled. This size control strategy has been recently illustrated by Owen and coworkers,[70] who used the reactivity of substituted thiourea precursors to tune the size of NCs of a number of metal sulfides, including $Cu_{2-x}S$. The authors demonstrated that increasing the thiourea reactivity produces a higher concentration of smaller NCs, as a result of faster monomer formation rates and, consequently, faster nucleation rates.

We propose that the dramatic impact of the $Sn(DDT)_xBr_y$ complexes on the formation of $Cu_{2-x}S$ NCs is also due to changes in the nucleation rates. However, in contrast to the examples discussed above, in the present case the nucleation is directly affected by the $Sn(DDT)_xBr_y$ complexes, which make it more difficult by increasing the activation energy for nucleation (Figure 5a). This additional nucleation barrier is imposed by the interaction between the $Sn(DDT)_xBr_y$ complexes and the [Cu-S] monomers, which transiently form heterometallic polynuclear Sn(IV)-Cu(I) thiolate complexes, as observed in the NMR measurements discussed above. This also implies that the higher the concentration of $Sn(DDT)_xBr_y$ complexes, the higher the nucleation barrier (Figure 5a). The monomer formation rates are not affected since they depend only on the thermolysis rates of the C-S bonds of the Cu-thiolate complexes. As a result, nucleation becomes the rate-limiting step, which impacts on both the size and shape of the product $Cu_{2-x}S$ NCs.

In the absence of $Sn(DDT)_xBr_y$ complexes, the activation energy for nucleation is low, but the monomer supply is limited by the C-S thermolysis rates. The polydisperse ensemble of relatively large nanoplatelets obtained in the absence of $SnBr_4$ (Figure 1a) suggests that the heating rates employed in our experiments are not sufficiently fast to induce a sudden burst of C-S thermolysis and monomer formation, thereby resulting in relatively few nucleation events spread over a wide temperature range. The addition of a small concentration of $SnBr_4$ (which is converted *in-situ* to $Sn(DDT)_xBr_y$ complexes) already significantly increases the activation energy for nucleation, delaying it until sufficiently high temperatures have been reached. The concentration of monomers produced by thermolysis of the Cu-DDT complexes will then be high, and a burst of nucleation followed by fast growth and depletion of the monomers becomes possible, leading to a high concentration of relatively small and monodisperse NCs (Figure 1b, 17 nm hexagonal bifrustums). Further increase in the concentration of added $SnBr_4$ leads to a higher concentration of *in-situ* generated $Sn(DDT)_xBr_y$ complexes, which make the nucleation rates increasingly lower, while keeping the monomer formation rates unaffected. As a result, the size of the product $Cu_{2-x}S$ NCs increases with increasing $Sn(DDT)_xBr_y$ (Figure 1), since fewer nuclei are formed under a constant monomer supply (Figure 5b,c). This also affects the morphology of the NCs, since facet development during growth and the final shape adopted by a colloidal NC are dictated by a balance between several driving forces,[1] as will be discussed below.

The growth rate of a given NC facet depends on its free-energy and on the total concentration of monomers

available for growth. At low monomer activities the overall growth rates are slow, and therefore the difference between different crystallographic facets are not significant (thermodynamically controlled growth regime).[1] Consequently, the NC will grow toward an equilibrium shape that minimizes the most its total free-energy, which implies that a relatively isotropic shape exposing low free-energy facets will be favored. In contrast, at high monomer activities the overall growth rates become fast, allowing the high free-energy facets to grow faster than the low free-energy ones, outcompeting them for the monomer supply. This leads to anisotropic morphologies (kinetically controlled growth regime).[1] Surfactants (ligands) modify the free-energy of specific facets through preferential binding, thereby depressing their growth rates relative to the facets that are less densely capped. This affects the shape evolution under both growth regimes.

Colloidal $Cu_{2-x}S$ NCs synthesized by thermolysis of Cu-DDT complexes have been shown to adopt a nearly spherical morphology at early growth stages or under slow growth conditions (*i.e.*, under thermodynamic control), and a hexagonal nanoplatelet morphology under fast growth conditions (*i.e.*, high concentrations and/or high temperatures).[6,26,29,38–40,63,64] This implies that the free-energies of the facets in the [010] and [001] directions (*viz.*, {101} and {221} for djurleite) are higher than that of the {100} facet. The different shapes of the $Cu_{2-x}S$ NCs obtained in the presence of different concentrations of $SnBr_4$ can be thus understood as a direct consequence of the impact of the *in-situ* generated $Sn(DDT)_xBr_y$ complexes on the nucleation rates. As discussed above, the nucleation rates decrease with increasing concentration of $Sn(DDT)_xBr_y$ complexes, which leads to an increasingly higher concentration of monomers available for growth, thereby enhancing the growth rates and favoring the formation of nanoplatelets with increasingly larger aspect ratios. The observation of a polydisperse ensemble of nanoplatelets in the absence of $SnBr_4$ (Figure 1a) can be ascribed to a combination of slow nucleation rates (limited by the monomer formation rates) spread over a wide temperature range and fast growth rates. The difference in the crystal structures of the differently shaped polyhedral $Cu_{2-x}S$ NCs (see above) can also be rationalized from this perspective, which implies that the low-chalcocite structure is thermodynamically favored, while the djurleite structure is kinetically favored. This is consistent with the fact that low-chalcocite is the thermodynamically stable crystal structure of Cu_2S below 105 °C.[41]

Tin(IV) compounds (*viz.*, Sn(acetylacetonate)Cl_2 and $SnCl_4$) have been previously reported to affect the shape of $Cu_{2-x}S$ NCs obtained by heating-up Cu(II)acetylacetonate in DDT, leading to the formation of either nanosheets or nanodisks, under conditions that would otherwise yield spherical NCs.[71-73] This effect has been tentatively ascribed to *in-situ* generated $[Sn_xS_y]$ species that were presumed to act as selective surfactants, thereby influencing the relative growth rates of different facets and thus altering the NC morphology.[71-73] No evidence was however provided for the presence of such species, either in the reaction medium or at the surface of the product $Cu_{2-x}S$ NCs. It is possible that the $Sn(DDT)_xBr_y$ complexes may also act as surfactants, but the NMR spectroscopy and elemental mapping results discussed above do not provide any evidence supporting the notion that the formation of nanoplatelets is induced by selective binding of these complexes to the top and bottom facets, since Sn was detected at very low concentrations and randomly distributed, regardless of the NC shape, and no Sn compounds were observed bound to the surface of the nanoplatelets. Surface bound $Sn(DDT)Br_3$ complexes were however observed in the solid-state ^{119}Sn NMR spectra of the bipyramid-shaped Cu_2S NCs. This suggests that $Sn(DDT)_xBr_y$ complexes preferentially bind to the {302}/{502} and {364} facets, possibly because these facets have a higher free-energy and are less densely capped with DDT molecules than the top and bottom {102} facets. This adsorption is however not strong enough to significantly depress the growth rates of the {302}/{502} and {364} facets, but slows it sufficiently down with respect to the {102} facets to allow the formation of bipyramid NCs, which require growth both in the [100] direction and in the [010] and [001] directions. This mild down-modulation of the {302}/{502} and {364} growth is nevertheless insufficient to counteract the dramatic increase in the growth rates brought about by further increase of the concentration of the $Sn(DDT)_xBr_y$ complexes, since this results in a large increase of the monomer concentrations.

CONCLUSIONS

We have shown that *in-situ* formed Sn(IV)-thiolate complexes can be used as shape directing agents that modulate the nucleation and growth rates of polyhedral $Cu_{2-x}S$ NCs. Several anisotropic polyhedral NCs were obtained with narrow size and shape distributions (*e.g.* hexagonal bifrustums and bipyramids, and hexagonal nanoplatelets with various aspect ratios), by solely changing the concentration of the additive $SnBr_4$, which is converted *in-situ* to Sn(IV)-thiolate complexes through a stepwise replacement of bromide by deprotonated thiols. The crystal structure of the product $Cu_{2-x}S$ NCs is observed to depend on the concentration of Sn(IV)-thiolate complexes, resulting in monoclinic low-chalcocite and monoclinic djurleite in the low- and high-concentration limits, respectively. Our results rule out that the impact of the Sn(IV)-thiolate complexes on the formation of $Cu_{2-x}S$ NCs is due to Sn incorporation in the growing NCs or to a surfactant effect. Instead, the Sn(IV)-thiolate complexes increase the $Cu_{2-x}S$ nucleation barrier, without affecting the precursor conversion rates. This influences both the nucleation and growth rates, and leads to a better separation between nucleation and growth, thereby decreasing the ensemble polydispersity. It also dictates the final shape and structure of the product $Cu_{2-x}S$ NCs by affecting the balance between the nucleation and growth rates under constant monomer

formation rates. In the low-concentration limit, the nucleation rates are relatively fast, leading to a high concentration of nuclei and a low concentration of monomers available for growth. This results in slow growth under thermodynamic control. The nucleation rates decrease with increasing concentration of Sn(IV)-thiolate complexes, which leaves an increasingly higher concentration of monomers available for growth. This progressively enhances the growth rates, thereby shifting the growth to the kinetically controlled regime.

The use of inorganic ligands as shape directing agents has not been extensively studied yet, and could possibly lead to novel NC morphologies and improved size control strategies. This could be beneficial for implementation of NCs in *i.e.* photovoltaic and photonic devices, for which well-defined building blocks are required to form highly-ordered thin layers of individual NCs. In combination with topotactic cation exchange reactions, this could boost the importance of the synthetic strategy developed in this work, giving rise to tailor-made NCs and NC solids with novel functionalities, which may prove beneficial for a number of applications.

ASSOCIATED CONTENT

Supporting Information. Additional figures and supplementary discussion. This material is available free of charge *via* the Internet at http://pubs.acs.org.

AUTHOR INFORMATION

Corresponding Author

*E-mail: (C.d.M.D.) c.demello-donega@uu.nl

ACKNOWLEDGMENTS

W.v.d.S. and C.d.M.D. acknowledge financial support from the division of Chemical Sciences (CW) of the Netherlands Organization for Scientific Research (NWO) under grant number ECHO.712.012.001. M.B. also gratefully acknowledges NWO for funding the NMR infrastructure (Middle Groot program, grant number 700.58.102). S.B. acknowledges financial support from the European Research Council (ERC Starting Grant # 335078-COLOURATOMS).

REFERENCES

1. Donega, C. d. M. Synthesis and Properties of Colloidal Heteronanocrystals. *Chem. Soc. Rev.* **2011**, *40*, 1512–1546.

2. Kovalenko, M. V; Manna, L.; Cabot, A.; Hens, Z.; Talapin, D. V; Kagan, C. R.; Klimov, V. I.; Rogach, A. L.; Reiss, P.; Milliron, D. J.; *et al.* Prospects of Nanoscience with Nanocrystals. *ACS Nano* **2015**, *9*, 1012-1057.

3. Talapin, D. V.; Lee, J. S.; Kovalenko, M. V.; Shevchenko, E. V. Prospects of Colloidal Nanocrystals for Electronic and Optoelectronic Applications. *Chem. Rev.* **2010**, *110*, 389–458.

4. Grim, J. Q.; Manna, L.; Moreels, I. A Sustainable Future for Photonic Colloidal Nanocrystals. *Chem. Soc. Rev.* **2015**, *44*, 5897-5914.

5. Shirasaki, Y.; Supran, G.; Bawendi, M.; Bulović, V. Emergence of Colloidal Quantum-Dot Light-Emitting Technologies. *Nat. Photonics* **2012**, *7*, 13–23.

6. van der Stam, W.; Berends, A. C.; Donega, C. d. M. Prospects of Colloidal Copper Chalcogenide Nanocrystals. *ChemPhysChem* **2016**, *17*, 559-581.

7. Zhang, Y.; Xie, C.; Su, H.; Liu, J.; Pickering, S.; Wang, Y.; Yu, W. W.; Wang, J.; Wang, Y.; Hahm, J.; *et al.* Employing Heavy Metal-Free Colloidal Quantum Dots in Solution-Processed White Light-Emitting Diodes. *Nano Lett.* **2011**, *11*, 329–332.

8. Kolny-Olesiak, J.; Weller, H. Synthesis and Application of Colloidal $CuInS_2$ Semiconductor Nanocrystals. *ACS Appl. Mater. Interfaces* **2013**, *5*, 12221–12237.

9. Luther, J. M.; Jain, P. K.; Ewers, T.; Alivisatos, A. P. Localized Surface Plasmon Resonances Arising from Free Carriers in Doped Quantum Dots. *Nat. Mater.* **2011**, *10*, 361–366.

10. Burda, C.; Chen, X.; Narayanan, R.; El-Sayed, M. A. Chemistry and Properties of Nanocrystals of Different Shapes. *Chem. Rev.* **2005**, *105*, 1025–1102.

11. Zhao, Y.; Pan, H.; Lou, Y.; Qiu, X.; Zhu, J.; Burda, C. Plasmonic $Cu_{2-x}S$ Nanocrystals: Optical and Structural Properties of Copper-Deficient Copper(I) Sulfides. *J. Am. Chem. Soc.* **2009**, *131*, 4253–4261.

12. Zhuang, Z.; Peng, Q.; Zhang, B.; Li, Y. Controllable Synthesis of Cu_2S Nanocrystals and Their Assembly into a Superlattice. *J. Am. Chem. Soc.* **2008**, *130*, 10482–10483.

13. Xie, Y.; Riedinger, A.; Prato, M.; Casu, A.; Genovese, A.; Guardia, P.; Sottini, S.; Sangregorio, C.; Miszta, K.; Ghosh, S.; *et al.* Copper Sulfide Nanocrystals with Tunable Composition by Reduction of Covellite Nanocrystals with Cu^+ Ions. *J. Am. Chem. Soc.* **2013**, *135*, 17630–17637.

14. Page, M.; Niitsoo, O.; Itzhaik, Y.; Cahen, D.; Hodes, G. Copper Sulfide as a Light Absorber in Wet-Chemical Synthesized Extremely Thin Absorber (ETA) Solar Cells. *Energy Environ. Sci.* **2009**, *2*, 220–223.

15. Wu, Y.; Wadia, C.; Ma, W.; Sadtler, B.; Alivisatos, A. P. Synthesis and Photovoltaic Application of Copper (I) Sulfide Nanocrystals. *Nano Lett.* **2008**, *8*, 2551–2555.

16. Xie, Y.; Carbone, L.; Nobile, C.; Grillo, V.; D'Agostino, S.; Sala, F. Della; Giannini, C.; Altamura, D.; Oelsner, C.; Kryschi, C.; *et al.* Metallic-like Stoichiometric Copper Sulfide Nanocrystals: Phase-and Shape-Selective Synthesis, Near-Infrared Surface Plasmon Resonance Properties, and Their Modeling. *ACS Nano* **2013**, *7*, 7352–7369.

17. Kriegel, I.; Rodríguez-Fernández, J.; Wisnet, A.; Zhang, H.; Waurisch, C.; Eychmüller, A.; Dubavik, A.; Govorov, A. O.; Feldmann, J. Shedding Light on Vacancy-Doped Copper Chalcogenides: Shape-Controlled Synthesis, Optical Properties, and Modeling of Copper Telluride Nanocrystals with near-Infrared Plasmon Resonances. *ACS Nano* **2013**, *7*, 4367–4377.

18. Dorfs, D.; Härtling, T.; Miszta, K.; Bigall, N. C.; Kim, M. R.; Genovese, A.; Falqui, A.; Povia, M.; Manna, L. Reversible Tunability of the Near-Infrared Valence Band Plasmon Resonance in $Cu_{2-x}Se$ Nanocrystals. *J. Am. Chem. Soc.* **2011**, *133*, 11175–11180.

19. Liu, Y.; Deng, Y.; Sun, Z.; Wei, J.; Zheng, G.; Asiri, A. M.; Khan, S. B.; Rahman, M. M.; Zhao, D. Hierarchical Cu_2S Microsponges Constructed from Nanosheets for Efficient Photocatalysis. *Small* **2013**, *9*, 2702–2708.

20. Vinokurov, K.; Elimelech, O.; Millo, O.; Banin, U. Copper Sulfide Nanocrystals Level Structure and Electrochemical Functionality towards Sensing Applications. *ChemPhysChem* **2016**, *17*, 675–680.

21. Hsu, S.; Bryks, W.; Tao, A. R. Effects of Carrier Density and Shape on the Localized Surface Plasmon Resonances of $Cu_{2-x}S$ Nanodisks. *Chem. Mater.* **2012**, *24*, 3765–3771.

22. Wolf, A.; Härtling, T.; Hinrichs, D.; Dorfs, D. Synthesis of Plasmonic $Cu_{2-x}Se$@ZnS Core@Shell Nanoparticles. *ChemPhysChem* **2016**, *17*, 717–723.

23. van der Stam, W.; Rabouw, F. T.; Vonk, S. J. W.; Geuchies, J. J.; Ligthart, H.; Petukhov, A. V.; Donega, C. d. M. Oleic Acid-Induced Atomic Alignment of ZnS Polyhedral Nanocrystals. *Nano Lett.* **2016,** *16*, 2608-2614..

24. Reifsnyder, D. C.; Ye, X.; Gordon, T. R.; Song, C.; Murray, C. B. Three-Dimensional Self-Assembly of Chalcopyrite Copper Indium Diselenide Nanocrystals into Oriented Films. *ACS Nano* **2013**, *7*, 4307–4315.

25. van der Stam, W.; Gantapara, A. P.; Akkerman, Q. A.; Soligno, G.; Meeldijk, J. D.; van Roij, R.; Dijkstra, M.; Donega, C. d. M. Self-Assembly of Colloidal Hexagonal Bipyramid- and Bifrustum-Shaped ZnS Nanocrystals into Two-Dimensional Superstructures. *Nano Lett.* **2014**, *14*, 1032–1037.

26. Kruszynska, M.; Borchert, H.; Bachmatiuk, A.; Rümmeli, M. H.; Büchner, B.; Parisi, J.; Kolny-Olesiak, J. Size and Shape Control of Colloidal Copper(I) Sulfide Nanorods. *ACS Nano*, **2012**, *6*, 5889–5896.

27. Sigman, M.; Ghezelbash, A.; Hanrath, T.; Saunders, A. E.; Lee, F.; Korgel, B. A. Solventless Synthesis of Monodisperse Cu_2S Nanorods, Nanodisks, and Nanoplatelets. *J. Am. Chem. Soc.* **2003**, *125*, 16050–16057.

28. Li, W.; Shavel, A.; Guzman, R.; Rubio-Garcia, J.; Flox, C.; Fan, J.; Cadavid, D.; Ibañez, M.; Arbiol, J.; Morante, J. R.; Cabot, A. Morphology Evolution of $Cu_{2-x}S$ Nanoparticles: From Spheres to Dodecahedrons. *Chem.Commun.* **2011**, 47, 10332–10334.

29. van der Stam, W.; Akkerman, Q. A.; Ke, X.; van Huis, M. A.; Bals, S.; Donega, C. d. M. Solution-Processable Ultrathin Size-and Shape-Controlled Colloidal $Cu_{2-x}S$ Nanosheets. *Chem. Mater.* **2015**, *27*, 283–291.

30. Beberwyck, B. J.; Surendranath, Y.; Alivisatos, A. P. Cation Exchange: A Versatile Tool for Nanomaterials Synthesis. *J. Phys. Chem. C* **2013**, *117*, 19759–19770.

31. Gupta, S.; Kershaw, S. V.; Rogach, A. L. 25th Anniversary Article: Ion Exchange in Colloidal Nanocrystals. *Adv. Mater.* **2013**, *25*, 6923–6944.

32. Li, H.; Zanella, M.; Genovese, A.; Povia, M.; Falqui, A.; Giannini, C.; Manna, L. Sequential Cation Exchange in Nanocrystals: Preservation of Crystal Phase and Formation of Metastable Phases. *Nano Lett.* **2011**, *11*, 4964–4970.

33. van der Stam, W.; Berends, A. C.; Rabouw, F. T.; Willhammar, T.; Ke, X.; Meeldijk, J. D.; Bals, S.; Donega, C. d. M. Luminescent $CuInS_2$ Quantum Dots by Partial Cation Exchange in $Cu_{2-X}S$ Nanocrystals. *Chem. Mater.* **2015**, *27*, 621–628.

34. Ha, D.-H.; Caldwell, A. H.; Ward, M. J.; Honrao, S.; Mathew, K.; Hovden, R.; Koker, M. K. A.; Muller, D. A.; Hennig, R. G.; Robinson, R. D. Solid–Solid Phase Transformations Induced through Cation Exchange and Strain in 2D Heterostructured Copper Sulfide Nanocrystals. *Nano Lett.* **2014**, *14*, 7090–7099.

35. Luther, J. M.; Zheng, H.; Sadtler, B.; Alivisatos, A. P. Synthesis of PbS Nanorods and Other Ionic Nanocrystals of Complex Morphology by Sequential Cation Exchange Reactions. *J. Am. Chem. Soc.* **2009**, *131*, 16851–16857.

36. van der Stam, W.; Bladt, E.; Rabouw, F. T.; Bals, S.; Donega, C. d. M. Near-Infrared Emitting $CuInSe_2/CuInS_2$ Dot Core/Rod Shell Heteronanorods by Sequential Cation Exchange. *ACS Nano* **2015**, *9*, 11430–11438.

37. de Trizio, L.; Manna, L. Forging Colloidal Nanostructures via Cation Exchange Reactions. *Chem. Rev.* **2016**, acs.chemrev.5b00739.

38. Kuzuya, T.; Tai, Y.; Yamamuro, S.; Sumiyama, K. Synthesis of Copper and Zinc Sulfide Nanocrystals *via* Thermolysis of the Polymetallic Thiolate Cage. *Sci. Technol. Adv. Mater.* **2005**, *6*, 84–90.

39. Bryks, W.; Wette, M.; Velez, N.; Hsu, S.; Tao, A. R. Supramolecular Precursors for the Synthesis of Anisotropic Cu_2S Nanocrystals. *J. Am. Chem. Soc.* **2014**, *136*, 6175–6178.

40. Nørby, P.; Johnsen, S.; Iversen, B. B. *In Situ* X-Ray Diffraction Study of the Formation, Growth, and Phase Transition of Colloidal $Cu_{2-x}S$ Nanocrystals. *ACS Nano* **2014**, *8*, 4295–4303.

41. Evans, H. Crystal Structure of Low Chalcocite. *Nature* **1971**, *232*, 69–70.

42. Pearson, R. G. Absolute Electronegativity and Hardness: Application to Inorganic Chemistry *Inorg. Chem.* **1988**, *27*, 734–740.

43. Chang, J.; Waclawik, E. R. Controlled Synthesis of $CuInS_2$, Cu_2SnS_3 and Cu_2ZnSnS_4 Nano-Structures: Insight into the Universal Phase-Selectivity Mechanism. *CrystEngComm* **2013**, *15*, 5612–5619.

44. Wang, J.; Liu, P.; Seaton, C. C.; Ryan, K. M. Complete Colloidal Synthesis of Cu_2SnSe_3 Nanocrystals with Crystal Phase and Shape Control. *J. Am. Chem. Soc.* **2014**, *136*, 7954–7960.

45. Tan, J. M. R.; Lee, Y. H.; Pedireddy, S.; Baikie, T.; Ling, X. Y.; Wong, L. H. Understanding the Synthetic Pathway of a Single-Phase Quarternary Semiconductor Using Surface-Enhanced Raman Scattering: A Case of Wurtzite Cu_2ZnSnS_4 Nanoparticles. *J. Am. Chem. Soc.* **2014**, *136*, 6684–6692.

46. Fiechter, S.; Martinez, M.; Schmidt, G.; Henrion, W.; Tomm, Y. Phase Relations and Optical Properties of Semiconducting Ternary Sulfides in the System Cu–Sn–S. *J. Phys. Chem. Solids* **2003**, *64*, 1859–1862.

47. Kruszynska, M.; Parisi, J.; Kolny-Olesiak, J. Synthesis and Shape Control of Copper Tin Sulphide Nanocrystals and Formation of Gold–Copper Tin Sulphide Hybrid Nanostructures. *Zeitschrift für Naturforsch. A* **2014**, *69*, 2–6.

48. Kruszynska, M.; Borchert, H.; Parisi, J.; Kolny-Olesiak, J. Synthesis and Shape Control of $CuInS_2$ Nanoparticles. *J. Am. Chem. Soc.* **2010**, *132*, 15976–15986.

49. Protesescu, L.; Rossini, A. J.; Kriegner, D.; Valla, M.; Kergommeaux, A. de; Walter, M.; Kravchyk, K. V; Nachtegaal, M.; Stangl, J.; Malaman, B.; *et al.* Unraveling the Core-Shell Structure of Ligand-Capped Sn/SnO_x Nanoparticles by Surface-Enhanced Nuclear Magnetic Resonance, Mössbauer, and X-Ray Absorption Spectroscopies. *ACS Nano* **2014**, *8*, 2639–2648.

50. Mundus, C.; Taillades, G.; Pradel, A.; Ribes, M. A Sn Solid-State Nuclear Magnetic Resonance Study of Crystalline Tin Sulphides. *Solid-State NMR*, **1996**, *7*, 141–146.

51. Kovalenko, M. V.; Bodnarchuk, M. I.; Zaumseil, J.; Lee, J.-S.; Talapin, D. V. Expanding the Chemical Versatility of Colloidal Nanocrystals Capped with Molecular Metal Chalcogenide Ligands. *J. Am. Chem. Soc.* **2010**, *132*, 10085–10092.

52. Kovalenko, M. V.; Scheele, M.; Talapin, D. V. Colloidal Nanocrystals with Molecular Metal Chalcogenide Surface Ligands. *Science* **2009**, *324*, 1417–1420.

53. Rangan, K. K.; Trikalitis, P. N.; Canlas, C.; Bakas, T.; Weliky, D. P.; Kanatzidis, M. G. Hexagonal Pore Organization in Mesostructured Metal Tin Sulfides Built with $[Sn_2S_6]^{4-}$ Cluster. *Nano Lett.* **2002**, *2*, 513–517.

54. Gielen, M. Tin Chemistry: Fundamentals, Frontiers and Applications. *Wiley*, **2008**, ISBN: 978-0-470-51771-0

55. Günther, H. NMR Spectroscopy: Basic Principles, Concepts and Applications in Chemistry. *Wiley*, **2013**, ISBN: 978-3-527-33004-1.

56. Wang, X.; Sheng, T.-L.; Fu, R.-B.; Hu, S.-M.; Xiang, S.-C.; Wang, L.-S.; Wu, X.-T. Assembly of a Heterometallic Polynuclear Sn(IV)-Cu(I) Cluster Based on $Sn(edt)_2$ (edt = Ethane-1,2-Dithiolate) as a Metalloligand. *Inorg. Chem.* **2006**, *45*, 5236–5238.

57. Wang, L.-S.; Sheng, T.-L.; Wang, X.; Chen, D.-B.; Hu, S.-M.; Fu, R.-B.; Xiang, S.-C.; Wu, X.-T. Self-Assembly of Luminescent Sn(IV)/Cu/S Clusters Using Metal Thiolates as Metalloligands. *Inorg. Chem.* **2008**, *47*, 4054–4059.

58. Jiao, J.; Lee, M.; Barnes, E.; Hagaman, E. W. Sn NMR Chemical Shift Tensors in Anhydrous and Hydrated $Si_8O_{20}(SnMe_3)_8$ Crystals. *Magn. Reson. Chem.* **2008**, *46*, 690–692.

59. Turo, M. J.; Macdonald, J. E. Crystal-Bound *vs* Surface-Bound Thiols on Nanocrystals. *ACS Nano* **2014**, *8*, 10205–10213.

60. Dierick, R.; Broeck, F. Van den; Nolf, K. De; Zhao, Q.; Vantomme, A.; Martins, J. C.; Hens, Z. Surface Chemistry of $CuInS_2$ Colloidal Nanocrystals, Tight Binding of L-Type Ligands. *Chem. Mater.* **2014**, *26*, 5950–5957.

61. Shavel, A.; Ibáñez, M.; Luo, Z.; Roo, J. De; Carrete, A.; Dimitrievska, M.; Gencì, A.; Meyns, M.; Pérez-Rodríguez, A.; Kovalenko, M. V.; *et al.* Scalable Heating-Up Synthesis of Monodisperse Cu_2ZnSnS_4 Nanocrystals. *Chem. Mater.* **2016**, *28*, 720–726.

62. Espinet, P.; Lequerica, M. C.; Martín-Alvarez, J. M. Synthesis, Structural Characterization and Mesogenic Behavior of Copper (I) n-Alkylthiolates. *Chem. Eur. J.* **1999**, *5*, 1982–1986.

63. Han, W.; Yi, L.; Zhao, N.; Tang, A.; Gao, M.; Tang, Z. Synthesis and Shape-Tailoring of Copper Sulfide/Indium Sulfide-Based Nanocrystals. *J. Am. Chem. Soc.* **2008**, *130*, 13152–13161.

64. Li, S.; Wang, H.; Xu, W.; Si, H.; Tao, X.; Lou, S.; Du, Z.; Li, L. S. Synthesis and Assembly of Monodisperse Spherical Cu_2S Nanocrystals. *J. Colloid Interface Sci.* **2009**, *330*, 483–487.

65. Wang, L.; He, W.; Yu, Z. Transition-Metal Mediated Carbon–Sulfur Bond Activation and Transformations. *Chem. Soc. Rev.* **2013**, *42*, 599–621.

66. Barone, G.; Chaplin, T.; Hibbert, T. G.; Kana, A. T.; Mahon, M. F.; Molloy, K. C.; Worsley, I. D.; Parkin, I. P.; Price, L. S. Synthesis and Thermal Decomposition Studies of Homo- and Heteroleptic Tin(iv) Thiolates and Dithiocarbamates: Molecular Precursors for Tin Sulfides. *J. Chem. Soc. Dalt. Trans.* **2002**, *6*, 1085–1092.

67. Owen, J. S.; Chan, E. M.; Liu, H.; Alivisatos, A. P. Precursor Conversion Kinetics and the Nucleation of Cadmium Selenide Nanocrystals. *J. Am. Chem. Soc.* **2010**, *132*, 18206–18213.

68. Abe, S.; Čapek, R. K.; de Geyter, B.; Hens, Z. Tuning the Postfocused Size of Colloidal Nanocrystals by the Reaction Rate: From Theory to Application. *ACS Nano* **2012**, *6*, 42–53.

69. Rempel, J. Y.; Bawendi, M. G.; Jensen, K. F. Insights into the Kinetics of Semiconductor Nanocrystal Nucleation and Growth. *J. Am. Chem. Soc.* **2009**, *131*, 4479–4489.

70. Hendricks, M. P.; Campos, M. P.; Cleveland, G. T.; Plante, I. J.; Owen, J. S. A Tunable Library of Substituted Thiourea Precursors to Metal Sulfide Nanocrystals. *Science* **2015**, *348*, 1226–1230.

71. Li, X.; Shen, H.; Niu, J.; Li, S.; Zhang, Y.; Wang, H.; Li, L. S. Columnar Self-Assembly of Cu_2S Hexagonal Nanoplates Induced by Tin(IV)-X Complex as Inorganic Surface Ligand. *J. Am. Chem. Soc.* **2010**, *132*, 12778–12779.

72. Li, X.; Wang, M.; Shen, H.; Zhang, Y.; Wang, H.; Li, L. S. Inorganic Sn-X-Complex-Induced 1D, 2D, and 3D Copper Sulfide Superstructures from Anisotropic Hexagonal Nanoplate Building Blocks. *Chemistry* **2011**, *17*, 10357–10364.

73. Yi, L.; Gao, M. From Ultrathin Two-Dimensional Djurleite Nanosheets to One-Dimensional Nanorods Comprised of Djurleite Nanoplates: Synthesis, Characterization, and Formation Mechanism. *Cryst. Growth Des.* **2011**, *11*, 1109–1116.

74. Palenstijn, W. J.; Batenburg, K. J.; Sijbers, J. Performance Improvements for Iterative Electron Tomography Reconstruction Using Graphics Processing Units (GPUs). *J. Struct. Biol.* **2011**, *176*, 250–253.

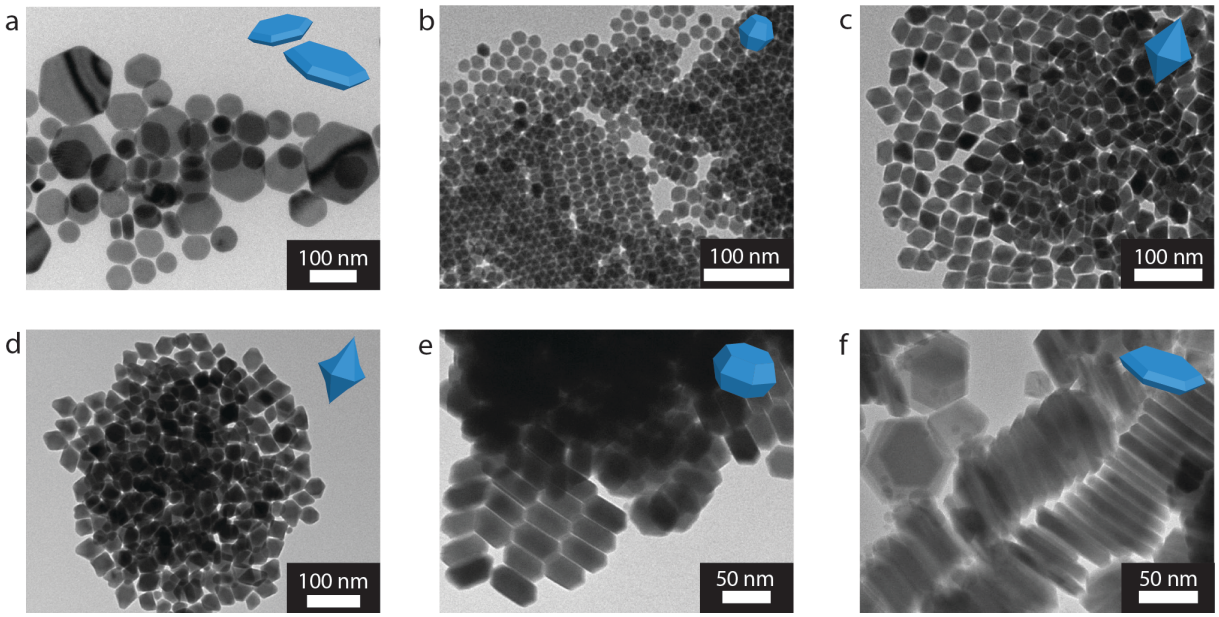

Figure 1. Representative Transmission Electron Microscopy (TEM) images of $Cu_{2-x}S$ nanocrystals synthesized with varying $SnBr_4$ concentrations under otherwise constant reaction conditions. The amount of $SnBr_4$ was the only variable, all other reaction parameters were kept constant. **(a)** Polydisperse $Cu_{2-x}S$ nanoplatelets synthesized in the absence of $SnBr_4$. **(b)** Monodisperse $Cu_{2-x}S$ bifrustum NCs (diameter: 17 nm) are obtained when a small amount of $SnBr_4$ is added (Cu:Sn 30:1). **(c)** A Cu:Sn ratio of 2:1 yields hexagonal bipyramids (28 nm wide, 38 nm long). **(d)** $Cu_{2-x}S$ NCs synthesized under Cu:Sn = 1:1. **(e)** Hexagonal nanoplatelets (25 nm thick, 50 nm wide) are obtained under Cu:Sn = 2:3. **(f)** Further increase of the Cu:Sn ratio to 1:2 leads to wider and thinner hexagonal nanoplatelets (80 nm by 10 nm).

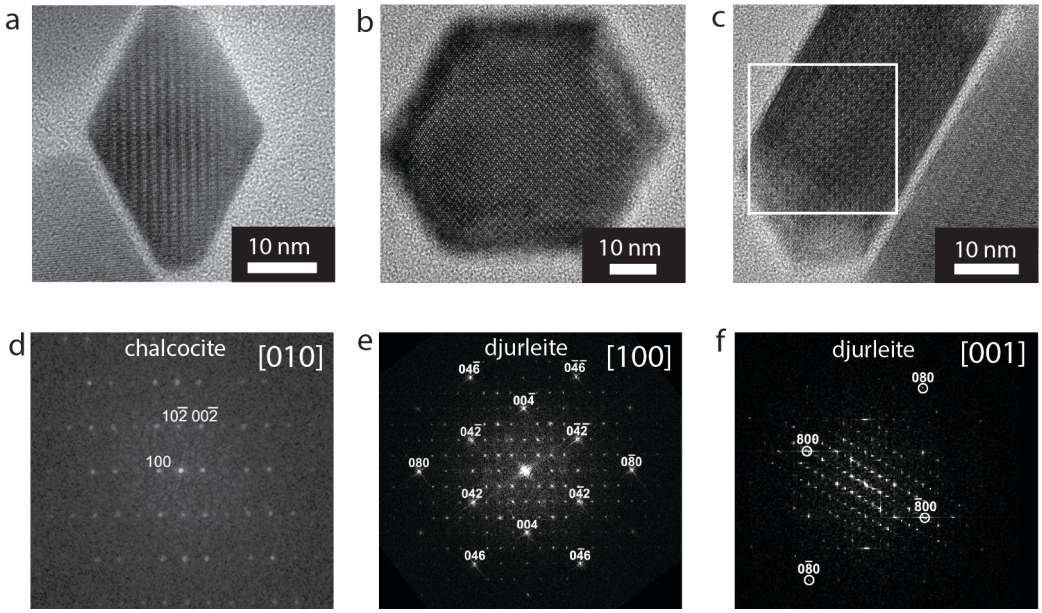

Figure 2. Structural analysis of the product $Cu_{2-x}S$ nanocrystals. High-Resolution Transmission Electron Microscopy (HRTEM) images of (a) hexagonal bipyramid $Cu_{2-x}S$ NCs and (**b**) low aspect ratio hexagonal $Cu_{2-x}S$ nanoplatelets viewed along the [100] direction and (**c**) along the [001] direction. The white square in c indicates the area of which the FFT pattern is displayed in panel f. (**d**) FFT pattern of the bipyramid NC displayed in panel a, showing characteristic diffraction spots of the low-chalcocite crystal structure viewed along the [010] zone axis. (**e**) FFT pattern of the NC displayed in panel b, showing characteristic diffraction spots of the djurleite crystal structure viewed along the [100] zone axis. (**f**) FFT pattern of a selected area (white square) of the NC displayed in panel c, showing characteristic diffraction spots of djurleite crystal structure, viewed along the [001] direction.

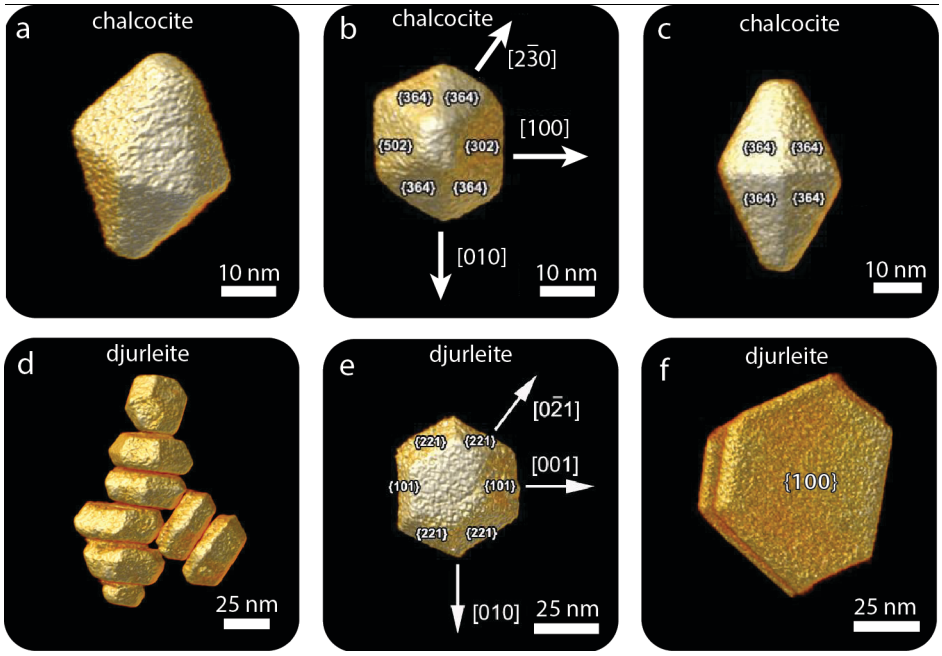

Figure 3. **Electron tomography reconstructions of polyhedral $Cu_{2-x}S$ nanocrystals.** (**a**) Low-chalcocite hexagonal bipyramid nanocrystal. (**b,c**) Facet indexation of a low-chalcocite hexagonal bipyramid (b) viewed along the [001] direction and (c) along the [010] direction. (**d**) Djurleite low aspect ratio hexagonal djurleite nanoplatelets, viewed along the [100] direction. (**e**) Facet indexation of a djurleite low aspect ratio hexagonal nanoplatelet viewed from the top. (**f**) Two high aspect ratio hexagonal nanoplatelets viewed from the top.

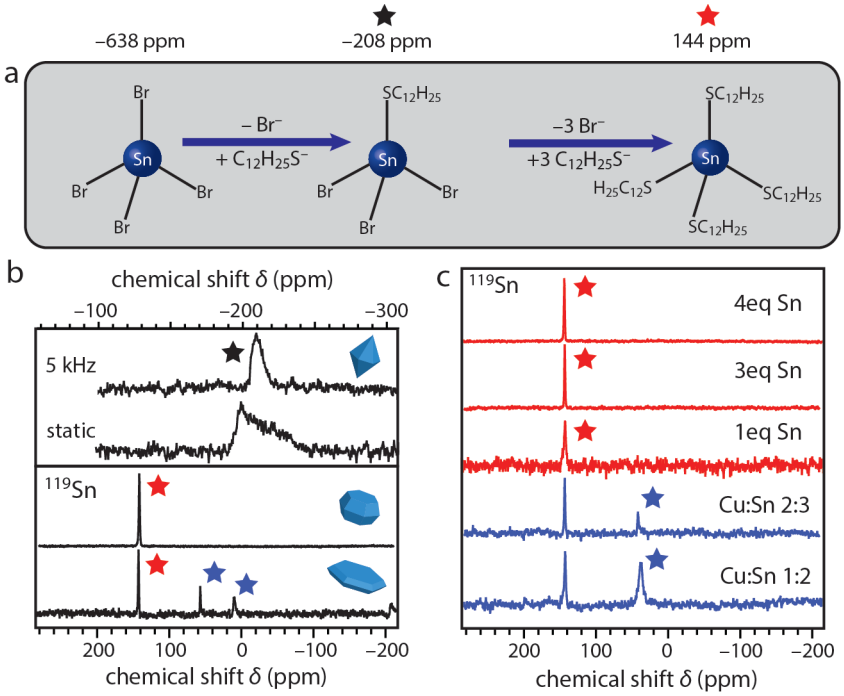

Figure 4. Solid-state and solution ^{119}Sn NMR spectra of polyhedral $Cu_{2-x}S$ nanocrystals and pre-nucleation reaction products. (**a**) Schematic representation of the Sn(IV)-thiolate complexes formed by stepwise replacement of bromide for deprotonated thiols. The chemical shift values for each structure are indicated at the top of the panel. (b) Solid-state ^{119}Sn NMR spectra of (top panel) hexagonal $Cu_{2-x}S$ bipyramids (with and without 5 kHZ MAS) and (bottom panel) low aspect ratio $Cu_{2-x}S$ nanoplatelets and high aspect ratio $Cu_{2-x}S$ nanoplatelets. The symbols refer to the Sn(IV)-thiolate complexes shown in panel a. (c) Solution ^{119}Sn NMR spectra of Blue lines, CuCl and $SnBr_4$ mixed in the same concentration and ratio used to synthesize the nanoplatelets. Red lines, different equivalents of $SnBr_4$ in DDT/OLAM.

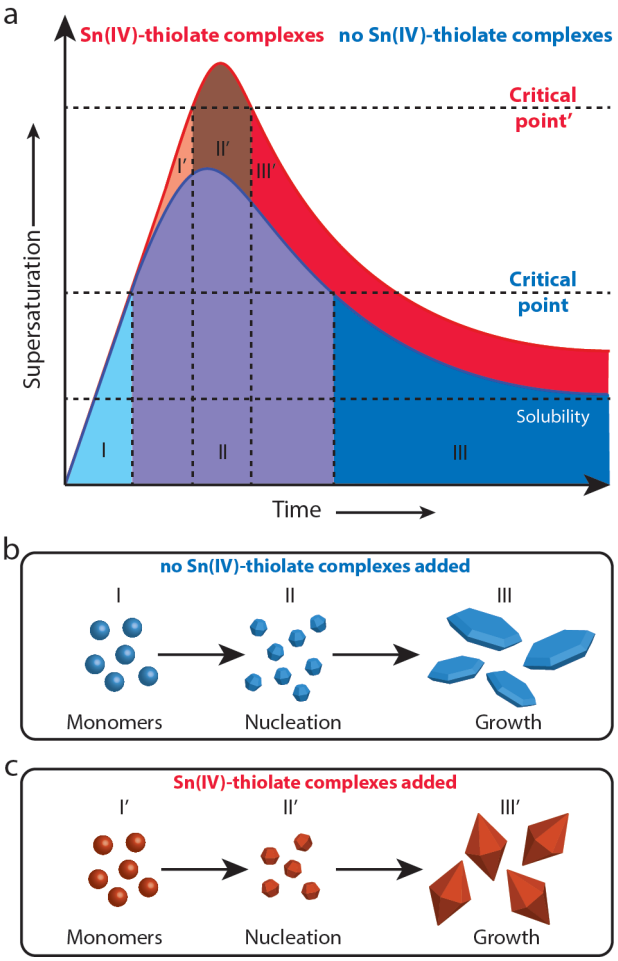

Figure 5. Tuning the nucleation and growth rates of $Cu_{2-x}S$ NCs by Sn-thiolate complexes. (**a**) La Mer plots of nucleation and growth of $Cu_{2-x}S$ nanocrystals (NCs) without (blue) and with Sn(IV)-additives (red). The addition of Sn(IV)-thiolate complexes to a $Cu_{2-x}S$ NC synthesis, results in an increase of the nucleation barrier and, as a result, nucleation and growth are well separated, resulting in polyhedral NCs with narrow size and shape distributions. (**b**,**c**) Schematic representations of the two $Cu_{2-x}S$ formation mechanisms. (**b**) Without Sn-additives, polydisperse $Cu_{2-x}S$ nanoplatelets are obtained and (**c**) with Sn-additives, well-defined polyhedral $Cu_{2-x}S$ NCs are formed.


Cu:Sn
2:1
Cu:Sn
2:3
Cu:Sn
1:2